Experimental characterization of fully-anisotropic equivalent fluids from normal incidence measurements

Théo Cavalieri, Melanie Nolan, Mathieu Gaborit, Jean-Philippe Groby

Experimental characterization of fully-anisotropic equivalent fluids from normal incidence measurements

Théo Cavalieri,[1, a)] Melanie Nolan,[2] Mathieu Gaborit,[1] and Jean-Philippe Groby[1, b)]

[1)] *Laboratoire d'Acoustique de l'Université du Mans (LAUM), UMR 6613, Institut d'Acoustique-Graduate School (IA-GS), CNRS, Le Mans Université, Avenue Olivier Messiaen, 72085 Le Mans, France*

[2)] *Acoustic Technology, Department of Electrical and Photonics Engineering Technical University of Denmark, Building 352, Ørsteds Plads, DK-2800 Kgs. Lyngby, Denmark*

(Dated: 23 July 2024)

Experimental validation remains crucial in the fields of acoustics materials and metamaterials. This study is based on a recent method, built upon the theoretical framework introduced by Terroir et al. in 2019, for characterizing three-dimensional anisotropic equivalent fluids, to which the experimental validation is paramount. This work focuses on the characterization of anisotropic fluids using a limited set of acoustic measurements in an impedance tube. In addition, the method demonstrates its ability to recover the Johnson-Champoux-Allard-Lafarge (JCAL) parameters as well as rotation angles and principal directions of an arbitrary equivalent fluid. These parameters are meaningful in understanding the acoustics of anisotropic porous materials. The recovery of these parameters is performed by a minimization procedure, which first recovers the thermo-acoustic properties of the medium, and secondly its visco-inertial properties. This technique showcases promise in effectively characterizing complex porous materials, underlining its potential for practical application.

[a)] Electronic mail: Theo.Cavalieri@univ-lemans.fr

[b)] Electronic mail: Jean-Philippe.Groby@univ-lemans.fr

1. INTRODUCTION

Verification and validation of theoretical frameworks are pivotal steps in ensuring the practical applicability and reliability of novel characterization methods for complex materials. In the fields of acoustics and meta-materials, the theoretical foundation for characterizing anisotropic porous materials has seen significant advancements[17,23,24,28]. However, experimental validation remains a critical step towards practical implementation and effectiveness of the proposed methodologies on real-world materials.

This study presents an experimental validation of a recently proposed method[26] aimed at characterizing fully anisotropic equivalent fluids (thermo-viscous fluids in the present case)[13,27]. More precisely, the present paper focuses on anisotropic porous materials in three dimensions (3D). The method is based on the principles of plane wave reflection and transmission through homogeneous samples, making it possible to extract the bulk modulus and all six components of the 3D symmetric anisotropic tensor of mass density.

In this experimental phase, we aim to demonstrate the method's efficacy through a series of characterization tests. The objective is to validate the extraction process of the anisotropic material parameters using a limited number of experimental measurements. Notably, the emphasis is placed on replicating real-world conditions to assess the method's robustness despite varying environmental factors, i.e., non-constant air properties, material thickness, measurement noise, and so on.

The present work uses the Johnson-Champoux-Allard-Lafarge (JCAL) theory[1,14,16], which describes the acoustic behavior of rigid-frame porous materials. This model serves as a reference in evaluating and validating experimental results when characterizing anisotropic porous materials. In order to recover the complete set of JCAL parameters, as well as principal directions of the mass density tensor, the particle swarm optimization[15,20] (PSO) minimization is performed. It stands as a powerful computational technique inspired by social behavior (among other minimization procedures), simulating the movement of particles seeking optimal solutions within bounded parameter spaces.

The following sections detail the experimental set-up, methodology, and findings derived from the validation process. This experimental validation establishes a strong foundation, making this method a valuable tool to characterize anisotropic porous materials (and by extension to equivalent fluids), making a substantial contribution to the fields of physical

acoustics and meta-material design.

The article is organized as follows. In Sec. 2, the propagation equations are briefly recalled to the reader. In Sec. 3 the recovery strategy is presented, starting from sets of scattering coefficients. From this point, the minimization strategy is described in order to recover the JCAL parameters and rotation angles. Details are also provided on the samples used in the study. Then, in Sec. 4 the efficiency of the procedure is demonstrated in the case of sound propagation through anisotropic equivalent fluids. All seven material parameters (6 coefficients of the symmetric density tensor and the bulk modulus) are accurately retrieved. They provide insight on the orientation of the material micro-structure through the recovery of the three principal directions and principal densities. The results and the validation of the method are finally discussed in Sec. 5. Additional data is provided on the characterization of a theoretical material in App. A, about the convergence of the method App. B, the pre-processing steps App. C, and the recovered parameters in App. D.

2. FORMULATION OF THE PROBLEM

In this section, the governing equations of the acoustic wave propagation in a general anisotropic homogeneous fluid layer are reminded, see Fig. 1. The layer has the thickness L and its constitutive material has the bulk modulus B and symmetric mass density tensor $\boldsymbol{\rho}$. In the reference Cartesian coordinate system $\mathcal{R}_0$ with position coordinates $\mathbf{x} = (x_1, x_2, x_3)$, the mutually parallel plane boundaries Γ_0 and Γ_L of the layer are at the positions $x_3 = 0$ and $x_3 = L$ respectively. The layer is surrounded on both sides $x_3 \leq 0$ and $x_3 \geq L$ by a homogeneous isotropic fluid. Here, the analysis is performed in the linear harmonic regime at the angular frequency ω with the implicit time dependence $\mathrm{e}^{-\mathrm{i}\omega t}$. In this system, the pressure and particle velocity fields $(P, \mathbf{V})$ in the layer are governed by the equations of mass and momentum conservation:

$$\mathrm{i}\omega P/B = \nabla \cdot \mathbf{V} \quad \text{and} \quad \mathrm{i}\omega \boldsymbol{\rho} \cdot \mathbf{V} = \nabla P \,. \tag{1}$$

Equations (1) testify that the anisotropy of the material is accounted for by the tensor character of its mass density $\boldsymbol{\rho} \in \mathbb{C}^{3\times3}$. For passive media, the mass density tensor $\boldsymbol{\rho}$ is symmetric, that is $\boldsymbol{\rho}^\top = \boldsymbol{\rho}$ where $^\top$ denotes non-conjugated transposition. In particular, the Cartesian coordinate system $\mathcal{R}_\rho$ of its principal directions with coordinates $(O, x_I, x_{I\!I}, x_{I\!I\!I})$

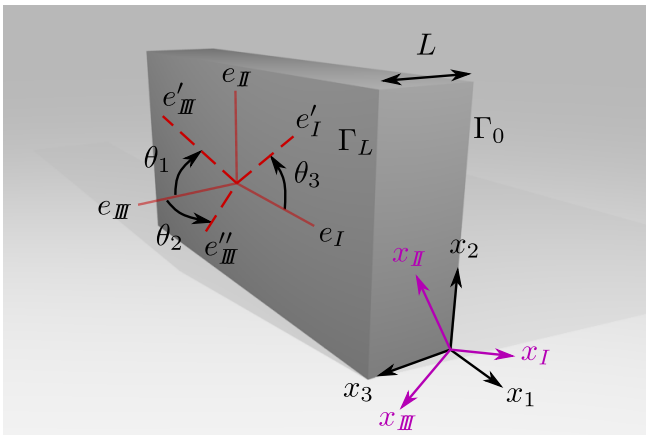

FIG. 1. (Color online) Conceptual view of the homogeneous anisotropic fluid layer of thickness L. The principal directions of the anisotropic fluid are denoted by (x_I, x_{II}, x_{III}). The interfaces of the fluid are Γ_0 and Γ_L.

can be defined so that the density matrix is diagonal in this system. In other words, the density tensor can be written as $\boldsymbol{\rho} = \boldsymbol{\rho}^\star = \mathbf{diag}\,(\rho_I, \rho_{II}, \rho_{III})$ in $\mathcal{R}_\rho$, where ρ_I, ρ_{II} and ρ_{III} are the principal mass densities. As a result, when expressed in the reference coordinate system $\mathcal{R}_0$, the mass density tensor reads $\boldsymbol{\rho} = \mathbf{R}\boldsymbol{\rho}^\star\mathbf{R}^\top$ where $\mathbf{R} = \mathbf{R}_3\,(\theta_{III})\,\mathbf{R}_2\,(\theta_{II})\,\mathbf{R}_1\,(\theta_I)$ is the rotation matrix between the two coordinate systems, with $\mathbf{R}_1$, $\mathbf{R}_2$, $\mathbf{R}_3$ being elementary matrices of rotations and θ_I, θ_{II} and θ_{III} the roll, pitch, and yaw angles. They are components of the set $\mathcal{A} = \{\theta_I, \theta_{II}, \theta_{III}\} \subset \mathbb{R}^3$. Moreover, it is worth recalling that, as effective properties, the bulk modulus B and mass density tensor $\boldsymbol{\rho}$ are complex-valued and frequency-dependent. As described in Ref. 26, the introduction of the symmetric tensor $\boldsymbol{H} = \boldsymbol{\rho}^{-1}$ is more convenient for the solution of both the direct and inverse problems. Note in particular that $\boldsymbol{H} = \mathbf{R}\boldsymbol{H}^\star\mathbf{R}^\top$ in the reference coordinate system $\mathcal{R}_0$, such as $\boldsymbol{H}^\star = \mathbf{diag}\,(1/\rho_I, 1/\rho_{II}, 1/\rho_{III}) = \mathbf{diag}\,(h_I, h_{II}, h_{III})$. The recovery of the six elements of the symmetric tensor $\boldsymbol{H}$ is thus completely equivalent to that of the symmetric tensor $\boldsymbol{\rho}$ tensor. The elements along the diagonal of $\boldsymbol{H}$ are denoted $h_{i=j}$ while the extra-diagonal components of the tensor are $h_{i\neq j}$.

3. MATERIALS AND METHODS

3.1. Retrieval of the effective properties from scattering coefficients

Contrary to the recovery procedure presented in Ref. 26, where reflection and transmission coefficients were assumed to be measurable at various angles of incidence, impedance tube measurement only provides reflection and transmission coefficients at normal incidence. Instead of varying the angle of incidence, samples of different orientations have thus to be placed in the impedance tube. Anechoic terminations being imperfect in practice, also leading to possible unexpected reflections at the impedance tube end, the method proposed in Ref. 18 based on the scattering matrix will be preferred to the one proposed in Ref. 24 based on the transfer matrix method. Once estimated, the material parameters will be marked by the superscript †. Whatever the upstream recovery method, the characteristic impedance Z and wavenumber k along the normal direction of the sample are recovered from the reflection R and transmission T coefficients as

$$Z^\dagger = Z_0 \sqrt{\frac{(1+R)^2 - T^2}{(1-R)^2 - T^2}}\,, \tag{2a}$$

$$\mathrm{e}^{\mp \mathrm{i} k^\dagger L} = \frac{1}{T}\left(1 + \frac{Z_0 \mp Z^\dagger}{Z_0 \pm Z^\dagger} R\right)\,, \tag{2b}$$

where $Z^\dagger = (B/h)^{1/2}$ and $k^\dagger = \omega\,(Bh)^{-1/2}$, and Z_0 is the impedance of the air in the impedance tube accounting for the thermo-viscous losses[25]. While the sign in Eq. (2a) is actually determined by the passivity constraint $\mathrm{Re}(Z^\dagger) \geq 0$, both signs in Eq. (2b) are physically sound. However, inverting $\mathrm{e}^{-\mathrm{i}k^\dagger L}$ is preferred here since the propagative waves in the same direction as the incident one usually carry more energy than the contra-propagative ones. While a single measurement is required to recover the bulk modulus from $B^\dagger = \omega Z^\dagger / k^\dagger$, six samples of different orientations have to be measured in order to recover the six upper elements of the symmetric tensor $\boldsymbol{H}$ from $h^\dagger = \omega / k^\dagger Z^\dagger$. The first three samples are naturally chosen to be oriented along the three axis of the reference coordinate system $\mathcal{R}_0$ (see Fig. 1), i.e., x_1, x_2, and x_3 in order to recover $h^\dagger_{11}$, $h^\dagger_{22}$, and $h^\dagger_{33}$ respectively as well as the bulk modulus $B^\dagger$. In order to recover the three remaining extra-diagonal elements, three additional samples are taken outside the reference coordinate system. These samples are taken from each of the three planes (x_2, O, x_3), (x_1, O, x_3), and (x_1, O, x_2), respectively corresponding to rotations θ_i around x_i as shown in Fig. 1. The reconstructed normal

elements $h'^{\dagger}_{33}$, $h''^{\dagger}_{33}$, and $h'^{\dagger}_{11}$, are related to h_{ij}, via the relations

$$\begin{cases} h'^{\dagger}_{33} = h^{\dagger}_{22}\sin^2\theta_1 + h^{\dagger}_{33}\cos^2\theta_1 + h_{23}\sin 2\theta_1 \ , \\ h''^{\dagger}_{33} = h^{\dagger}_{11}\sin^2\theta_2 + h^{\dagger}_{33}\cos^2\theta_2 - h_{13}\sin 2\theta_2 \ , \\ h'^{\dagger}_{11} = h^{\dagger}_{11}\cos^2\theta_3 + h^{\dagger}_{22}\sin^2\theta_3 - h_{12}\sin 2\theta_3 \ , \end{cases} \tag{3}$$

where $\{(i,j)\in\{1,2,3\}^2 \,|\, j\geq i\}$ and from which we immediately recover the extra-diagonal terms $h^{\dagger}_{i\neq j}$ with the prior knowledge of the diagonal terms $h^{\dagger}_{i=j}$.

To summarize: six different samples, the orientation of three of them being along the reference coordinate system $\mathcal{R}_0$ and the orientation of the three remaining ones lying in the three planes (x_i, O, x_j) are required to recover the elements of the symmetric tensor $\boldsymbol{H}$. The bulk modulus is recovered six times and may either be averaged or used as validation of the measurements.

3.2. Minimization strategy

The anisotropic equivalent fluid is now assumed to be a porous material, the skeleton of which is supposed to be acoustically rigid and impervious. The normalized diagonal elements $\rho_0 h^{\dagger}_J$ in each principal direction, $J\in\{I, II, III\}$, and the normalized bulk modulus $B^{\dagger}/B_0$ read as[14,16]

$$\begin{aligned} \rho_0 h^{\dagger}_J &= \frac{\phi}{\tau^{\infty}_J}\left(1 + \frac{\mathrm{i}\nu\phi}{\omega K^0_J \tau^{\infty}_J}\sqrt{1 - \frac{\mathrm{i}\omega}{\nu}\left(\frac{2\tau^{\infty}_J K^0_J}{\phi\Lambda_J}\right)^2}\right)^{-1} , \\ \frac{B^{\dagger}}{B_0} &= \frac{1}{\phi}\left[\gamma - (\gamma-1)\left(1 + \frac{\mathrm{i}\nu'\phi}{\omega\Theta^0}\sqrt{1 - \frac{\mathrm{i}\omega}{\nu'}\left(\frac{2\Theta^0}{\phi\Lambda'}\right)^2}\right)^{-1}\right]^{-1} , \end{aligned} \tag{4}$$

where γ is the specific heat ratio, $\nu = \eta/\rho_0$ the kinematic viscosity, η the dynamic viscosity, and ρ_0 the density of the saturating fluid. The visco-inertial JCAL parameters τ^{∞}_J, K^0_J, and Λ_J are respectively the high-frequency tortuosities, viscous characteristic lengths, and visco-static permeabilities in each principal direction $J\in\{I, II, III\}$. The 9 visco-inertial JCAL parameters constitute the set $\mathcal{Q}\subset\mathbb{R}^9$. In addition, ϕ, Λ', and Θ^0 are respectively the open porosity, the thermal characteristic length, and the thermo-static permeability, constituting the set $\mathcal{Q}'\subset\mathbb{R}^3$. From Eq. (4), we notice that ϕ is the sole geometric parameter which is common to both of the effective quantities $\mathbf{H}$ and B.

3.2.1. Cost functions and objectives

The goal of the present strategy is thus to recover the set of parameters $\mathcal{P} = \{\mathcal{Q}, \mathcal{Q}', \mathcal{A}\}$, from the knowledge of $h_{ij}^{\dagger}(\omega)$ and $B^{\dagger}(\omega)$ over a given frequency range. In a first instance, and in order to estimate the open porosity ϕ, the following cost function is minimized

$$C_1(\mathcal{Q}') := B_0^{-1} \left\| B^{\dagger} - B(\mathcal{Q}') \right\| \ , \tag{5}$$

with the constraint $\phi \in]0,1[$, and where the operator $\|\bullet\|$ is the $\mathcal{L}^2$-norm. After having obtained the set of parameters $\mathcal{Q}'_{\text{guess}} = \text{argmin}\, C_1$, the focus is on $\mathcal{Q}$ and $\mathcal{A}$, namely the visco-inertial JCAL parameters and the rotation angles. The values of ϕ_{guess}, Λ'_{guess}, and Θ^0_{guess} will be used to bound the search space during the minimization of C_2, as given in Eq. (7). For this purpose the following cost function is minimized:

$$C_2(\mathcal{P}) := \rho_0 \sum_{i \geq j} \left\| h_{ij}^{\dagger} - h_{ij}(\mathcal{Q}, \mathcal{A}, \phi) \right\| + C_1(\mathcal{Q}') \ . \tag{6}$$

In addition, the mass density tensor is expressed $\mathbf{H} = \mathbf{R}(\mathcal{A}) \mathbf{diag}\left[h_J(\mathcal{Q}, \phi)\right] \mathbf{R}^{\top}(\mathcal{A})$ and the minimization constraints on the parameters are set as

$$\begin{cases} \phi & \in \ [\phi_{\text{guess}} - \varepsilon, \phi_{\text{guess}} + \varepsilon] \cap]0,1[\ , \\ \Lambda' & \in \ [\Lambda'_{\text{guess}}/2, 2\Lambda'_{\text{guess}}] \ , \\ \Theta^0 & \in \ [\Theta^0_{\text{guess}}/2, 2\Theta^0_{\text{guess}}] \ , \\ \tau_J^{\infty} & \geq 1 \ , \\ \Lambda_J & \leq \Lambda' \ , \\ K_J^0 & \leq \Theta^0 \ , \\ \theta_J & \in [0, \pi/2[\ , \end{cases} \tag{7}$$

with $J \in \{I, I\!I, I\!I\!I\}$ and $\varepsilon = 0.05$.

The minimization of both cost functions $C_i(\mathcal{P})$ is performed using the PSO method[15,20]. The search space is bounded by the aforementioned limits of the JCAL parameters $\{\mathcal{Q}', \mathcal{Q}\}$ and rotation angles $\mathcal{A}$, and initialized uniformly with 20 particles (candidate solutions) per parameter. In order to ensure the robustness of the method, the minimization is ran 10 times with uniformly randomized individuality and sociality coefficients, i.e., parameters of the PSO. Finally, the set of parameters $\mathcal{P}$ that best minimizes $C_2(\mathcal{P})$ is chosen as the optimal solution. The routines are implemented within MATLAB® via the function `particleswarm` from the *Global Optimization Toolbox*.

3.2.2. Non-uniqueness of solutions

It turns out that although the method presented here enables the effective parameters of anisotropic fluids to be found faithfully, it presents a constraint with regard to the uniqueness of the solutions. In this short section, the non-uniqueness of the solutions is discussed.

Firstly, since the propagation problem at hand is symmetric and reciprocal in all three directions of space: the rotation angles are π-periodic. Secondly, it is not possible to uniquely determine the viscous parameters of the set $\mathcal{Q}$ and the rotation angles $\mathcal{A}$. In other words, assigning parameters to the principal direction $\mathbf{e}_J$ for a given set of angles $\mathcal{A}$ is in essence equivalent to assigning this same set of parameters to the direction $\mathbf{e}_{J'} \neq \mathbf{e}_J$ by admitting an additional rotation of $\pm\pi/2$ around the perpendicular axis $\mathbf{e}_J \times \mathbf{e}_{J'}$.

This will lead the minimization procedure to permute the direction-dependent JCAL parameters as well as providing solutions where the rotation angles are modulo $\pi/2$. For these reasons, it is sufficient to define the rotation angles on $[0, \pi/2[$ as a regularization, thus forcing the direction $\mathbf{e}_1 = (1, 0, 0)$ to be in the octant $(+, +, -)$ after transformation.

In conclusion, although the sets $\mathcal{Q}$ and $\mathcal{A}$ are closely dependent and non-unique, the method is able to recover the coefficients of the mass density tensor reliably.

3.3. Sample preparation

Different materials are tested with the present characterization procedure. First, 3D-printed porous materials, and finally glass-wool.

On the one hand, 3D-printed materials that are manufactured from additive techniques such as fused deposition modeling or stereo-lithography can be designed at the microscopic level. In this way, they can exhibit anisotropic features, making them excellent candidates to test the present characterization method[29]. As described in previous works, these techniques constitute an efficient way of manufacturing by-design acoustic porous absorbers[6,7,10,12] and meta-materials[8,11]. In the present case, a micro-trellis structure is chosen, which classically results from rectangular infill patterns with fused filament deposition[7]. This structure is a primitive tetragonal (tP) Bravais lattice[2], and can be described through its representative volume element (RVE). The trellis is isotropic in the horizontal plane (O, x_1, x_2), which makes the whole material transverse isotropic. Theoretical and experimental investigations

of the acoustics of 3D-printed materials[6,7,9–11,26] have shown that porous materials built with additive manufacturing techniques can be modeled numerically through the a two-scale asymptotic homogenization procedure[3,22,29]. The JCAL parameters and the effective properties of this material are obtained from finite-element method (FEM), using the commercial software COMSOL Multiphysics® for various filling fractions. These results will serve as a reference to which the reconstructed parameters will be compared to. To study the results given by the characterization method, samples are printed with the following in-fill percentages: 10 %, 20%, 30 %, 50 %.

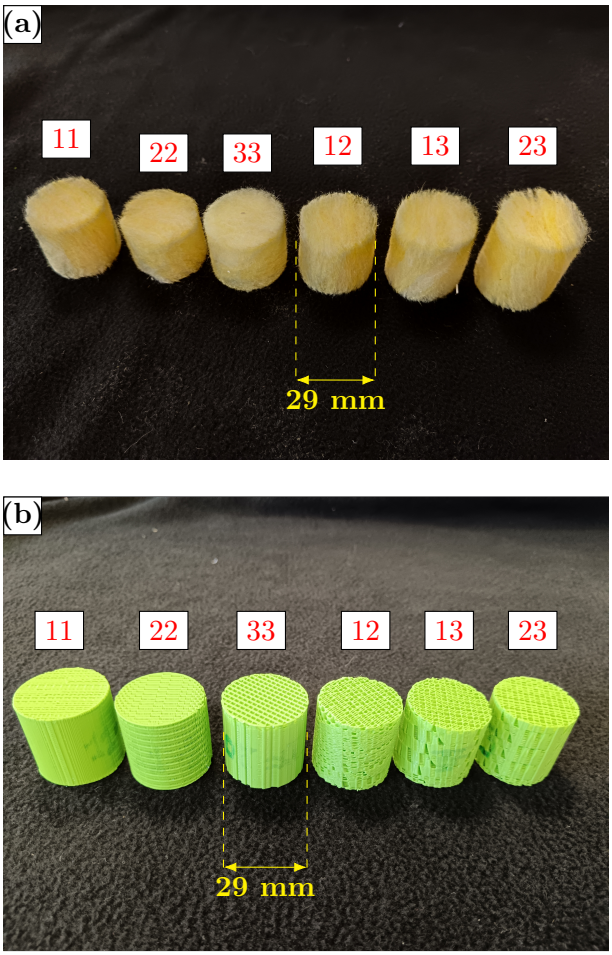

FIG. 2. (Color online) Photographs of some of the samples used for the characterization process. The samples in panel **(a)** are glass-wool, and these on panel **(b)** are a 3D-printed micro-trellis.

On the other hand, glass-wool is a fibrous material that results from the stretching of molten glass. This is commonly obtained by heating sand and recycled glass at high temperatures which is then forced through thin holes, resulting in fibers. The latter are then mixed

with a binder, resulting in a relatively rigid and highly porous mat of interconnected glass fibers. In the present case, the glass-wool samples are carved out of larger panels provided by Saint-Gobain Ecophon.

The samples are tested in a cylindrical impedance tube of diameter $d = 30\,\text{mm}$. For glass-wool, the samples are cut in the 6 different directions (as described earlier in Sec. 3 3.1) using a band saw and a cylindrical knife. For the 3D-printed micro-trellis, the samples are directly printed with the desired orientations.

4. RESULTS

In this section the retrieval procedure of JCAL parameters is applied to different materials: a 3D-printed micro-trellis, and glass-wool which is known for its acoustic absorption properties. Furthermore, a theoretical fully-anisotropic porous material is presented in the Appendix A, and the convergence of the parameters is shown in Appendix B.

In order to obtain the scattering coefficients of the tested samples, a four-microphone impedance tube[19] is used. The tube diameter is $d = 30\,\text{mm}$, which allows to measure up to the plane-wave frequency limit $f \approx 6700\,\text{Hz}$. The measurements were performed on samples of various thickness, which is trivially accounted for in the inversion procedure via Eq. (2b). The chosen source signal is a logarithmic swept sine with time duration $T = 1\,\text{s}$, over the frequency range of interest 100 Hz – 7000 Hz. The measured pressure signals are then averaged over 30 iterations. The frequency range and pre-processing steps are detailed in the App. C. The figures will present the reconstructed effective properties (inverse mass density tensor and bulk modulus), and the recovered JCAL parameters are given in App. D.

4.1. 3D-printed micro-trellis

In this first example, we focus on a 3D-printed micro-trellis, as described earlier. From the minimization results, it is observed that the reconstructed diagonal terms $h_{i=j}$ of the inverse mass density tensor are in good agreement with their experimental estimates, as shown in Fig. 3**(a,b)**. Moreover, the transverse isotropy of the material is clearly evidenced as $\mathbf{H}$ satisfies $h_{11} \approx h_{22} \neq h_{33}$. This translates in the micro-trellis having a higher apparent mass density in the transverse plane (O, x_1, x_2), than along the printing direction $\mathbf{e}_{\text{III}}$. In the

present case, the material was measured in its principal directions, meaning $\mathcal{R}_0 \equiv \mathcal{R}_\rho$. This implies that the extra-diagonal terms are very small in comparison to the diagonal terms, as visible in Fig. 3**(a)**, and one of the principal directions is along the vertical axis x_3 as in Fig. 3**(c)**.

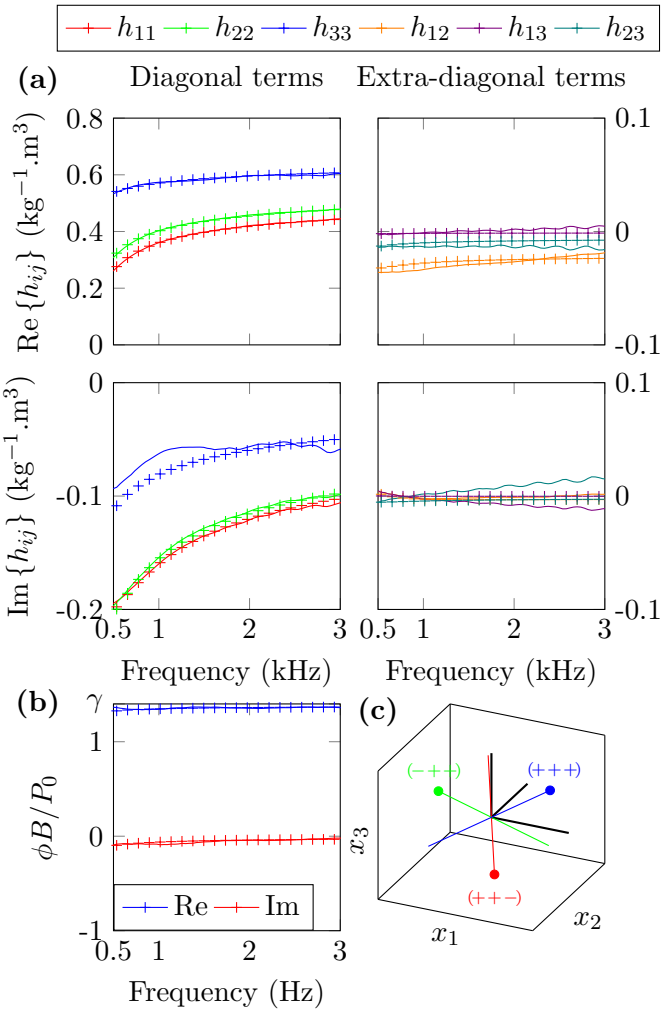

FIG. 3. (Color online) Measured (–) and reconstructed (+) inverse mass density tensor **(a)** and normalized bulk modulus **(b)**. The orientations of the principal directions are shown in **(c)**.

However, one could expect the reconstructed directions to be aligned with the principal axes of the system $\mathcal{R}_0$. Here again, as there is isotropy in the transverse plane (O, x_I, x_{II}), the mass density tensor admits a rotational invariance along x_{III}. In addition, while the extra-diagonal terms h_{13} and h_{23} are theoretically identical, this is not the case experimentally, leading the minimization routine to induce unnecessary rotations. Nevertheless, with the results provided in Fig. 3, all the meaningful information is retrieved:

- all seven properties (h_{ij} and B) of the equivalent fluid are correctly minimized,
- the material is shown to be transverse isotropic,
- one principal direction aligned with $\mathbf{e}_3$.

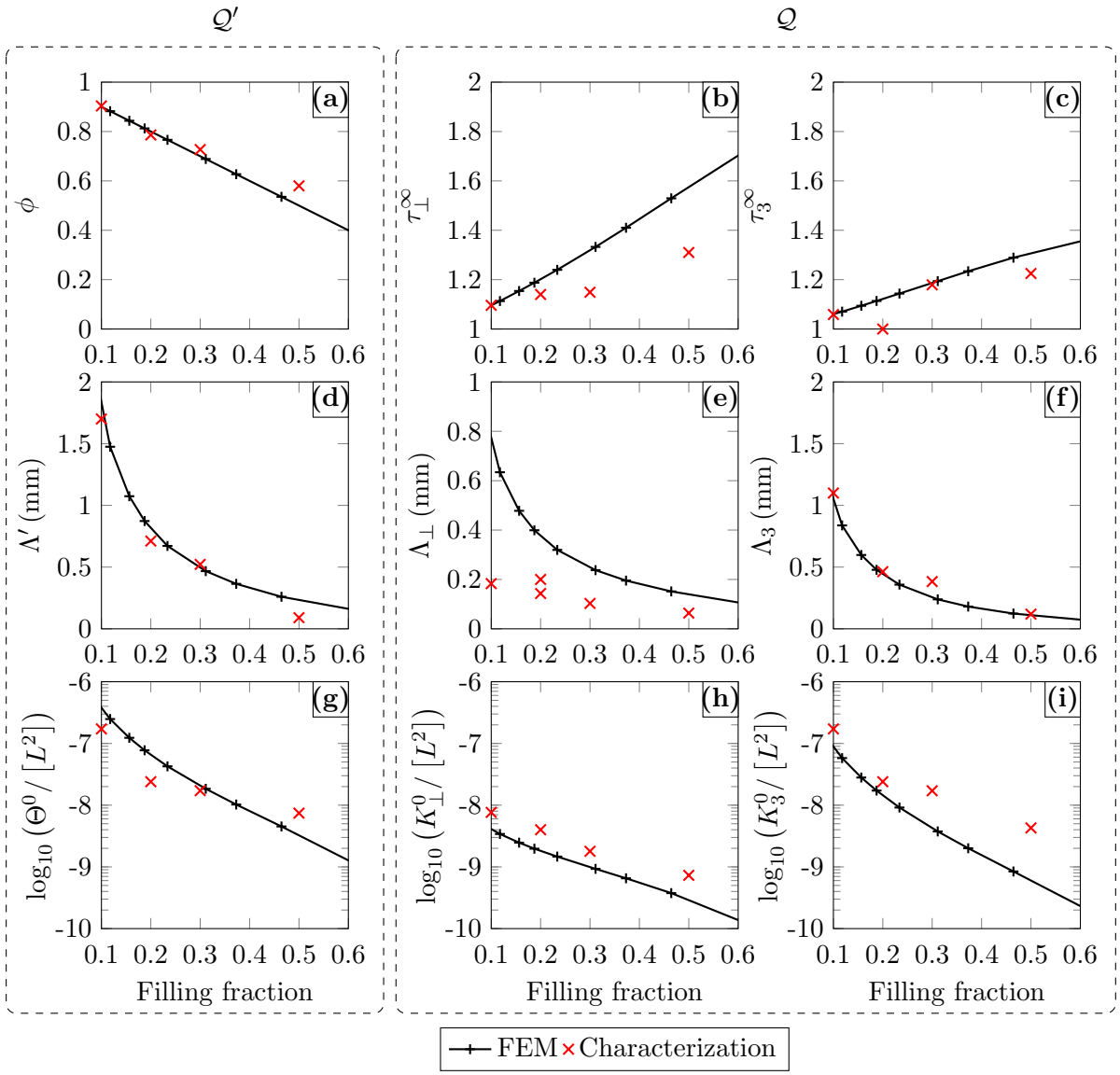

FIG. 4. (Color online) Comparison of JCAL parameters with respect to filling fraction. The FEM estimates are shown with black markers (+), and the characterized parameters are in red markers (×). The thermo-acoustic parameters $\mathcal{Q}'$ are displayed in **(a,d,g)**, and the visco-inertial parameters of $\mathcal{Q}$ are **(b,c,e,f,h,i)**.

The results provided by the characterization method are finally compared to numerical data

estimated by FEM. Figure 4 shows the recovered (red markers) and the numerical estimates (black markers) of the JCAL parameters with respect to the filling fraction. A good agreement is observed, although some discrepancies are noticeable. These are predominantly linked to manufacturing defects of 3D-printed porous materials. These defects include (but are not limited to) surface roughness of the filament and its ellipticity, macroscopic deformations due to thermal gradients and gravity, as well as changes of the filament's cross-section along the printing path[5,9,29].

It also appears that some parameters are better estimated than others: the set of recovered thermo-acoustic parameters $\mathcal{Q}'$ that minimize the cost functions are in good agreement with the numerical estimates, as visible on Fig. 4**(a,d,g)**, but this is less true for the visco-inertial parameters, which are harder to estimate. The increased difficulty in reconstructing the visco-inertial parameters $\mathcal{Q}$ comes from manufacturing defects, which are strongly direction-dependent. While the parameters $\mathcal{Q}'$ only depend on the scalar field of temperature inside the fluid phase, the parameters $\mathcal{Q}$ are liked to the distribution of the particle velocity within the fluid. The latter is quite sensitive to the presence of defects, such as surface roughness, pore clogging, and overall deformations of the solid phase. All these effects are detailed in Refs. 5 and 7.

In spite of the differences that lie between the reconstructed values and their theoretical estimates, we observe that these parameters do follow the same trends: the characteristic lengths and permeabilities decrease with respect to the filling fraction, while the tortuosities increase as the pores get smaller. Albeit the proposed method is able to recover the equivalent fluid properties of the micro-trellis material.

4.2. Glass-wool material

The method is now applied to the characterize a fibrous glass-wool material, which is usually considered to be isotropic with a high value of porosity. The recovered parameters are given in Tab. III: the high-frequency tortuosities τ_J^∞ are identical in all three directions of space, but the characteristic viscous lengths and visco-static permeabilities show some disparities in the different directions. As expected for classical fibrous materials the reconstruction provides $\tau_J^\infty \approx 1$ and $\phi \approx 1$. In addition to the JCAL parameters being in the range to what is commonly attributed to glass-wool, a great agreement is observed between

the measured and reconstructed effective properties, as shown in Fig. 5. In Fig. 5**(a)**, we observe that the material seems to be transverse isotropic from the real part of the diagonal mass densities, similarly to the micro-trellis. However, the extra-diagonal terms are not negligible, and the set of JCAL parameters lead to consider the material as anisotropic. In

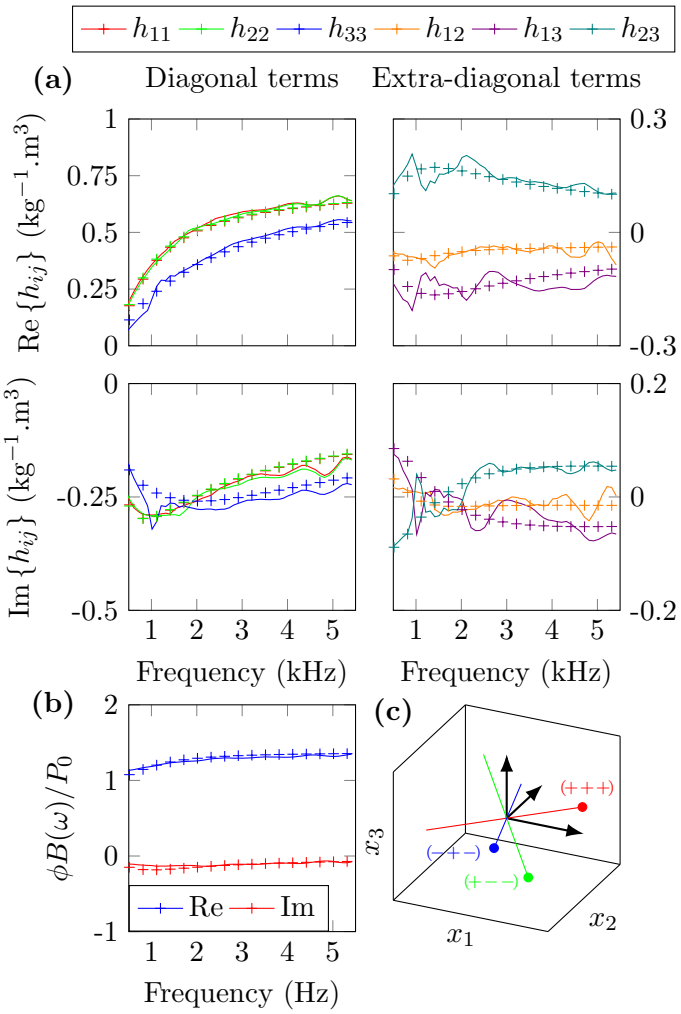

FIG. 5. (Color online) Measured (–) and reconstructed (+) inverse mass density tensor **(a)** and normalized bulk modulus **(b)**. The orientations of the principal directions are shown in **(c)**.

Fig. 6, binary images are shown to assess the differences in fiber arrangement in the horizontal plane. Qualitatively, the fibers are more intertwined and swirly in one direction than in the other, where they seem more longitudinal and parallel to each other. This is also evidenced by the 2D spatial Fourier transform $\mathcal{F}$ of the images, showing that the energy distribution of the spectrum is different in both cases, and in particular along the vertical axis, which reflects the alignment of the fibers, i.e., perfectly horizontal fibers would result

in $\mathcal{F}$ being a vertical line.

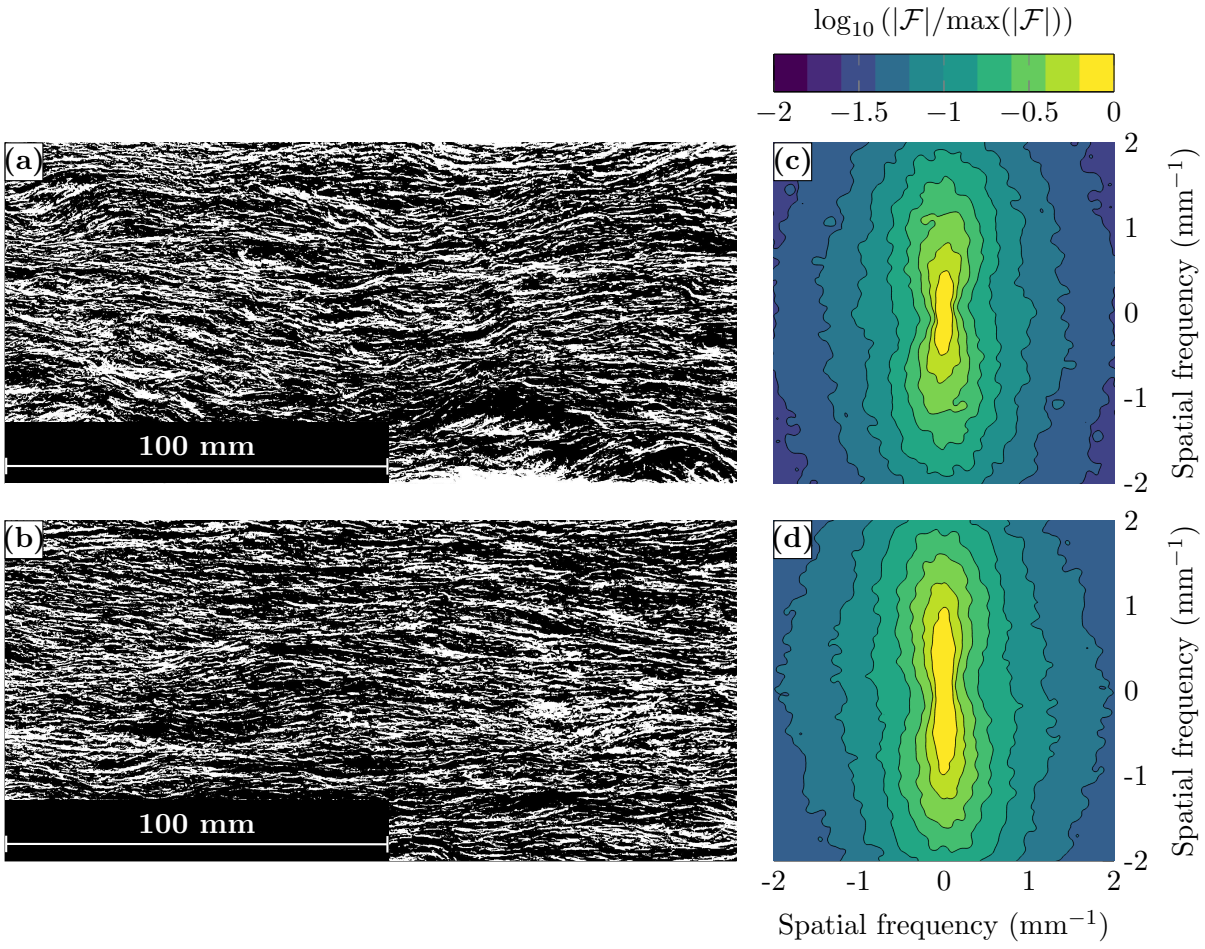

FIG. 6. (Color online) Binary images of cuts in glass-wool along directions $\mathbf{e}_1$ and $\mathbf{e}_2$, respectively in **(a)** and **(b)** evidencing discrepancies in fiber arrangement in the plane (O, x_1, x_2). Two-dimensional normalized spatial Fourier transform $\mathcal{F}$ of the cuts respectively in **(c)** and **(d)**.

Albeit, the set of recovered parameters, the principal directions of the material, and qualitative image analysis of the fiber arrangement lead to the conclusion that glass-wool panels are slightly anisotropic, especially in regard to the air-flow resistivity $\sigma = \eta/K^0$, which ranges from $4.8\,\mathrm{kPa.m^{-2}.s}$ to $28\,\mathrm{kPa.m^{-2}.s}$.

5. CONCLUSION

In this work, an experimental recovery of the effective properties of anisotropic fluids is presented. It follows the characterization method proposed in Ref. 26, using a limited set of

acoustic measurements to estimate the transport parameters of fully-anisotropic equivalent fluids. In the present study, the focus is on porous materials, which in the fields of acoustics are classically modeled as fluids with complex and frequency-dependent effective properties. Moreover, instead of considering the propagation of an oblique incident acoustic field on a homogeneous layer, we perform the characterization with plane waves at normal incidence on samples cut at different angles. This makes the method particularly well suited to existing acoustic characterization rigs, especially impedance tubes. A validation step is carried out on a theoretical fully-anisotropic material (presented in Appendix A and B), for which the proposed method is able to retrieve the parameters and rotation angles exactly.

On the first hand, 3D-printed micro-trellis with different filling fractions are studied, as their effective properties can be readily estimated by FEM. The experimental results were then windowed and filtered prior to being fed into the minimization routines. The results show that all parameters including the orientation of the principal directions can be retrieved accurately. Moreover, the method is able to recover the trends of the equivalent fluid's behavior for different filling fractions.

On the second hand, the method is tested on glass-wool, which is a very common material used in construction and which is known for its acoustic absorption capabilities. However, the method has evidenced differences in regard to the effective properties in the in-plane directions of glass-wool. The findings are supported with the cross-sectional cuts of glass-wool, showing that the interlacing of fibers can indeed differ in the horizontal plane. While some of the recovered parameters are consistent with what is expected from this material, glass-wool seems to display a slight anisotropy.

The results presented in this work illustrate the method's ability to reconstruct the properties and principal directions of an arbitrary homogeneous anisotropic fluid. In addition, it can be used as a tool to guide the design of complex acoustic media. Current research on acoustic treatments focuses on structured and multi-functional materials, such as meta-materials, which are commonly considered as equivalent fluids. The present method can be useful in assessing the quality of such materials, and in particular those that are 3D-printed.

Appendix A: Theoretical data

In this part, the method is validated using purely theoretical data, based on a simulated porous material as equivalent fluid. The simulated material is similar to that of Refs. 10, 12, and 26. The effective properties of the latter are estimated using a micro-macro approach[3,22,29], then arbitrary rotations are applied to the tensor of mass density.

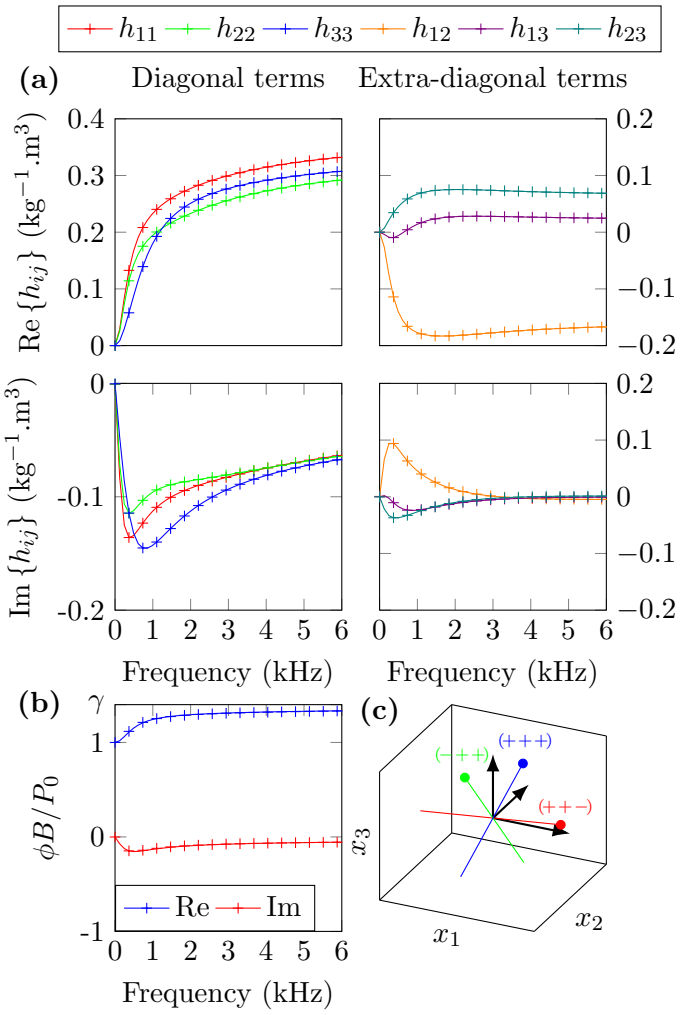

FIG. 7. (Color online) Theoretical (+) and reconstructed (–) inverse mass density tensor **(a)** and normalized bulk modulus **(b)**. The orientations of the principal directions are shown in **(c)**.

The propagation equations are used to determine the scattering coefficients of a plane wave on a fully-anisotropic porous material. The reconstructed effective parameters are shown in Fig. 7. In this configuration, all parameters $\mathcal{P}$ presented in Tab. I are retrieved exactly, and the cost function satisfies $C(\mathcal{P}) = \mathcal{O}(10^{-16})$. This is evidenced by the perfect

match between theoretical and reconstructed values of $h_{ij}^{\dagger}$ and $B^{\dagger}$ presented in Fig. 7.

Appendix B: Convergence of the method

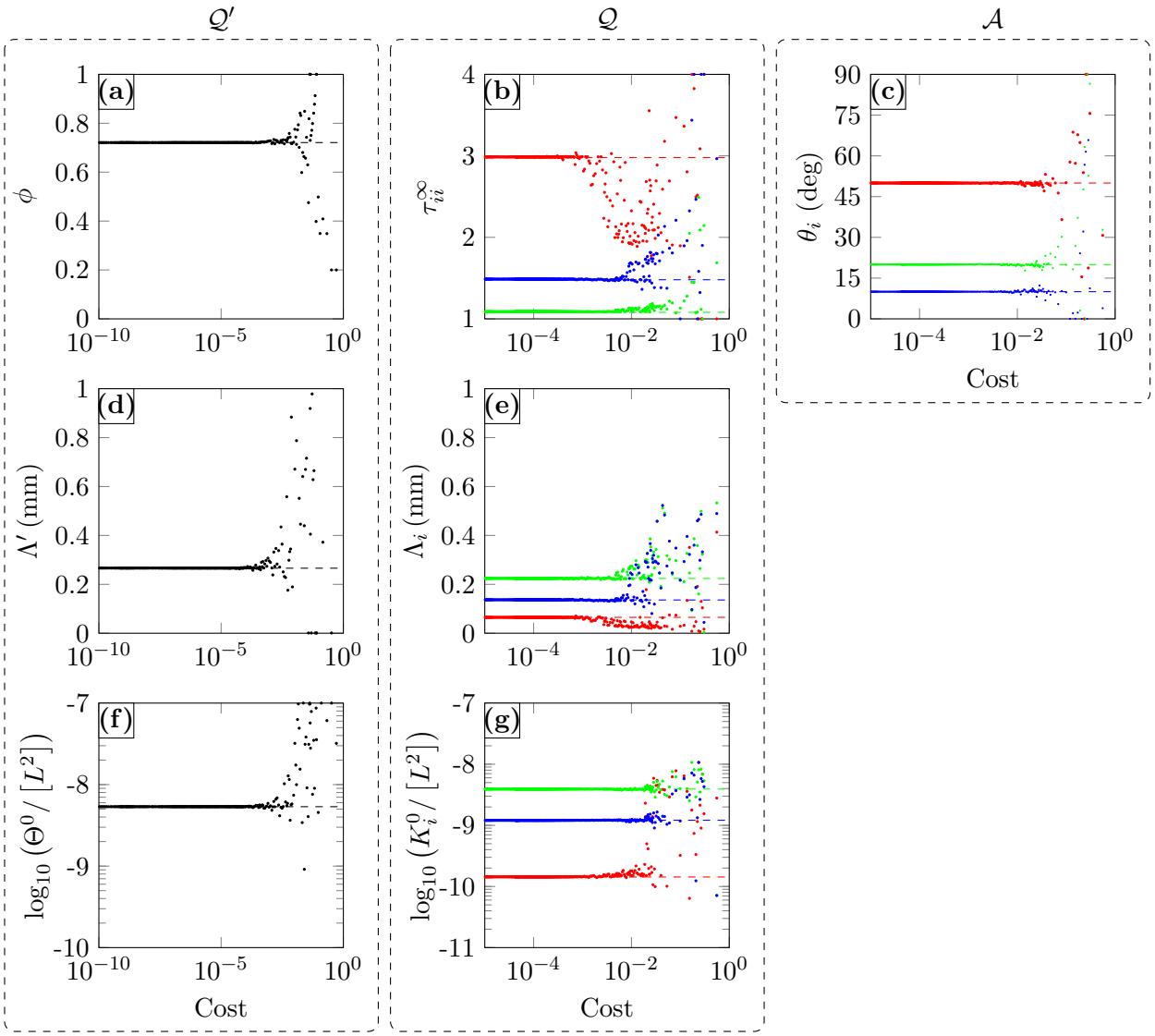

FIG. 8. (Color online) Convergence of parameters with respect to cost. The dashed lines represent the theoretical values, while the dots show the position of the particles during the PSO. The thermo-acoustic parameters are shown in the left column, the visco-inertial parameters in the center column, and the rotation angles in the right column.

The convergence of the parameters for the theoretical material can be observed in Fig. 8. The left column shows the convergence of the set of thermo-viscous parameters $\mathcal{Q}'$ with respect to the cost C_1. The center and right columns show the visco-inertial parameters and rotation angles respectively, this time with respect to the cost C_2. We observe that all parameters converge towards the expected value (represented by the dashed line), and some parameters converge faster than others, which is expected. For example this is the case for quasi-isotropic materials, where the non-diagonal terms of the inverse mass density tensor are non-zero, leading to inaccurate angle determination. Noisy data can also lead to inaccuracies and loss of stability in the recovery procedure. Finally, some parameters are more important than others in minimizing the cost functions such as the open porosity ϕ which strongly scales the bulk modulus and mass density of the equivalent fluid, as described in Eq. 4.

Appendix C: Pre-processing

As the effective parameters are estimated from the reflection and transmission coefficients via Eqs. (2b) and (2a), noise on the experimental data can lead to hectic behaviors of $\mathbf{H}$ and B. For this reason, the effective parameters are processed before recovering the JCAL parameters and principal directions.

In a first instance, the data is windowed in frequency. This is meant to disregard the frequencies for which the measurements are noisy (especially at low frequencies, determining f_{min}), and above the cut-off frequency of the impedance tube (determining f_{max}). Moreover, Biot resonances linked to elastic waves propagating inside the solid phase of the porous material[4] can disturb the recovery of effective parameters, as the JCAL model does not account for this phenomena. In this way, windowing is the first and most important step before the determination of the parameters $\mathcal{P}$.

Naturally, a second processing step consists in smoothing $\mathbf{H}$ and B. It is applied in order to reduce noise on the effective quantities and provide a better setting before applying the minimization routines. The experimental scattering coefficients are smoothed with a moving average filter[21] over 50 Hz.

The last step consists in under-sampling the experimental data. While this can sound unreasonable to the reader, it can be of great use to speed up the minimization procedures

without being detrimental to the quality of the reconstruction. As computing the cost functions requires the evaluation of $\mathcal{L}^2$-norms, reducing the number of frequency points can considerably shorten the computation time. In addition, as the quantities to be minimized (namely $h_{ij}^{\dagger}$ and $B^{\dagger}$) are smooth and continuous functions, down-sampling the experimental data is performed reasonably without loss of useful information.

Appendix D: Recovered parameters

	ϕ	Λ' (µm)	Θ^0 (nm^2)	τ^∞	Λ (µm)	K^0 (nm^2)	θ
Ω	0.721	266	5.357	–	–	–	–
$\mathbf{e}_{I}$	–	–	–	2.987	64.95	0.14	$\pi/18$
$\mathbf{e}_{II}$	–	–	–	1.089	224.3	3.92	$\pi/9$
$\mathbf{e}_{III}$	–	–	–	1.487	136.8	1.12	$5\pi/18$

TABLE I. Theoretical values of JCAL parameters and rotation angles of the simulated material.

	ϕ	Λ' (µm)	Θ^0 (nm^2)	τ^∞	Λ (µm)	K^0 (nm^2)	θ
Ω	0.786	711	24.03	–	–	–	–
$\mathbf{e}_{I}$	–	–	–	1.000	463	24.03	33.5°
$\mathbf{e}_{II}$	–	–	–	1.141	143	3.432	0°
$\mathbf{e}_{III}$	–	–	–	1.135	200	4.698	38.2°

TABLE II. Reconstructed values of JCAL parameters and rotation angles for the mirco-trellis with 20% filling fraction.

	ϕ	Λ' (µm)	Θ^0 (nm^2)	τ^∞	Λ (µm)	K^0 (nm^2)	θ
Ω	0.99	368	4.16	–	–	–	–
$\mathbf{e}_{I}$	–	–	–	1.010	99.5	1.655	43.8°
$\mathbf{e}_{II}$	–	–	–	1.000	368	3.752	0°
$\mathbf{e}_{III}$	–	–	–	1.000	56.9	0.642	32.9°

TABLE III. Reconstructed values of JCAL parameters and rotation angles for glass-wool.

ACKNOWLEDGEMENTS

The authors gratefully acknowledge the financial support of the METARoom Project No. ANR-18-CE08-0021 which is co-funded by A.N.R. and R.G.C., as well as the Independent Research Fund Denmark, under DFF-International Postdoctoral Grant 1031-00012. The authors acknowledge Vicent Romero-García, Charlie Bricault, and Lino Morin for their contributions to this work. Finally, the authors thank Saint-Gobain Ecophon for providing some of the samples used in the experimental validation.

DATA AVAILABILITY

The data that support the findings of this study are available upon request to the corresponding authors.

CONFLICTS OF INTEREST

The authors declare no conflict of interest.

CREDIT AUTHORSHIP CONTRIBUTION STATEMENT

T. C.: Software, Methodology, Validation, Formal analysis, Investigation, Resources, Data Curation, Writing - Original Draft, Writing - Review & Editing, Visualization. **M. N.:** Investigation, Methodology, Resources, Writing - Review & Editing. **M. G.:** Investigation, Methodology, Resources, Writing - Review & Editing, Supervision. **J.-P. G.:** Conceptualization, Methodology, Software, Validation, Formal analysis, Investigation, Resources, Data Curation, Writing - Original Draft, Writing - Review & Editing, Supervision, Project administration, Funding acquisition

REFERENCES

[1]J. Allard, R. Bourdier, and A. L'Esperance. Anisotropy effect in glass wool on normal impedance in oblique incidence. *Journal of Sound and Vibration*, 114(2):233–238, 1987.

[2]M. I. Aroyo. *International Tables for Crystallography: Space-group symmetry*, volume A. International Union of Crystallography, 2 edition, 2016.

[3]C. Auriault, J.-L. Boutin and C. Geindreau. *Homogenization of Coupled Phenomena in Heterogenous Media*, page 476. ISTE Ltd and Wiley, 2009.

[4]M. A. Biot. Mechanics of Deformation and Acoustic Propagation in Porous Media. *Journal of Applied Physics*, 33(4):1482–1498, 04 1962.

[5]J. Boulvert. *Traitements acoustiques á porosité contrôlée pour atténuation optimale (Translation: Acoustic treatments with controlled porosity for optimal attenuation)*. PhD thesis, Le Mans Université (France), 2020.

[6]J. Boulvert, T. Cavalieri, J. Costa-Baptista, L. Schwan, V. Romero-García, G. Gabard, E. R. Fotsing, A. Ross, J. N. Mardjono, and J.-P. Groby. Optimally graded porous material for broadband perfect absorption of sound. *Journal of Applied Physics*, 2019.

[7]J. Boulvert, J. Costa-Baptista, T. Cavalieri, M. Perna, E. R. Fotsing, V. Romero-García, G. Gabard, A. Ross, J. N. Mardjono, and J.-P. Groby. Acoustic modeling of micro-lattices obtained by additive manufacturing. *Applied Acoustics*, 164:107244, 2020.

[8]J. Boulvert, J. Costa-Baptista, T. Cavalieri, V. Romero-García, G. Gabard, E. R. Fotsing, A. Ross, M. Perna, J. Mardjono, and J.-P. Groby. Folded metaporous material for sub-wavelength and broadband perfect sound absorption. *Applied Physics Letters*, 117(25):251902, 2020.

[9]T. Cavalieri. *Design and fabrication of anisotropic and graded porous materials with embedded resonators for sound absorption*. PhD thesis, Le Mans Université, 2021.

[10]T. Cavalieri, J. Boulvert, G. Gabard, V. Romero-García, M. Escouflaire, J. Regnard, and J.-P. Groby. Graded and anisotropic porous materials for broadband and angular maximal acoustic absorption. *Materials*, 13, 2020.

[11]T. Cavalieri, J. Boulvert, V. Romero-García, G. Gabard, M. Escouflaire, J. Regnard, and J.-P. Groby. Rapid additive manufacturing of optimized anisotropic metaporous surfaces for broadband absorption. *Journal of Applied Physics*, 129:115102, 2021.

[12]T. Cavalieri, J. Boulvert, L. Schwan, G. Gabard, V. Romero-García, J.-P. Groby, M. Escouflaire, and J. N. Mardjono. Acoustic wave propagation in effective graded fully anisotropic fluid layers. *The Journal of the Acoustical Society of America*, 146 5:3400, 2019.

[13]J. Christensen and F. J. García de Abajo. Anisotropic metamaterials for full control of acoustic waves. *Phys. Rev. Lett.*, 108:124301, 2012.

[14]D. L. Johnson, J. Koplik, and R. Dashen. Theory of dynamic permeability and tortuosity in fluid saturated porous media. *J. Fluid Mech.*, 176:379–402, 1987.

[15]J. Kennedy and R. Eberhart. Particle swarm optimization. In *Proceedings of ICNN'95 - International Conference on Neural Networks*, volume 4, pages 1942–1948, Perth, WA, Australia, 1995. IEEE.

[16]D. Lafarge, P. Lemarinier, J.-F. Allard, and V. Tarnow. Dynamic compressibility of air in porous structures at audible frequencies. *J. Acoust. Soc. Am.*, 102:1995–2006, 1997.

[17]A. M. Nicolson and G. F. Ross. Measurement of the intrinsic properties of materials by time-domain techniques. *IEEE Trans. Instrum. Meas.*, 19:377–382, 1970.

[18]M. Niskanen, J.-P. Groby, A. Duclos, O. Dazel, J. C. Le Roux, N. Poulain, T. Huttunen, and T. Lähivaara. Deterministic and statistical characterization of rigid frame porous materials from impedance tube measurements. *J. Acoust. Soc. Am.*, 142:2407–2418, 2016.

[19]M. Niskanen, J.-P. Groby, A. Duclos, O. Dazel, J.-C. L. Roux, N. Poulain, T. Huttunen, and T. Lähivaara. Deterministic and statistical characterization of rigid frame porous materials from impedance tube measurements. *The Journal of the Acoustical Society of America*, 142 4:2407, 2017.

[20]M. Pedersen and A. Chipperfield. Simplifying Particle Swarm Optimization. *Applied Soft Computing*, 10(2):618–628, Mar. 2010.

[21]L. R. Rabiner and B. Gold. *Theory and application of digital signal processing*. Prentice-Hall, 18. [print.] edition, 1975.

[22]E. Sanchez-Palencia. *Non-Homogeneous Media and Vibration Theory*, volume 127 of *Lecture Notes in Physics*. Springer-Verlag, Berlin, Heidelberg, 1980.

[23]D. Smith, S. Schultz, P. Markoš, and C. M. Soukoulis. Determination of effective permittivity and permeability of metamaterials from reflection and transmission coefficients. *Phys. Rev. B*, 65:195104, 2002.

[24]B. H. Song and J. S. Bolton. A transfer-matrix approach for estimating the characteristic impedance and wave numbers of limp and rigid porous materials. *J. Acoust. Soc. Am.*, 107:1131–1152, 2000.

[25]M. Stinson. The propagation of plane sound waves in narrow and wide circular tubes, and generalization to uniform tubes of arbitrary cross-sectional shape. *J. Acoust. Soc. Am.*, 89:550–558, 1991.

[26]A. Terroir, L. Schwan, T. Cavalieri, V. Romero-García, G. Gabard, and J.-P. Groby. General method to retrieve all effective acoustic properties of fully-anisotropic fluid materials in three dimensional space. *J. Appl. Phys.*, 125:025114, 2019.

[27]D. Torrent and J. Sánchez-Dehesa. Anisotropic mass density by two-dimensional acoustic metamaterials. *New J. Phys*, 10:023004, 2008.

[28]W. B. Weir. Automatic measurement of complex dielectric constant and permeability at microwave frequencies. *Proc. IEEE*, 62:33–36, 1974.

[29]T. G. Zieliński, R. Venegas, C. Perrot, M. Červenka, F. Chevillotte, and K. Attenborough. Benchmarks for microstructure-based modelling of sound absorbing rigid-frame porous media. *Journal of Sound and Vibration*, 483:115441, 2020.